



# The visible light-driven photodegradation of dimethyl sulfide on S-doped TiO<sub>2</sub>: Characterization, kinetics, and reaction pathways



Yi-Hsing Lin<sup>a</sup>, Hsin-Ta Hsueh<sup>b</sup>, Chia-Wen Chang<sup>a</sup>, Hsin Chu<sup>a,\*</sup>

<sup>a</sup> Department of Environmental Engineering, National Cheng Kung University, 1 University Road, Tainan 701, Taiwan

<sup>b</sup> Department of Environmental Engineering and Sustainable Environment Research Laboratories, 1 University Road, Tainan 701, Taiwan

## ARTICLE INFO

### Article history:

Received 28 March 2016

Received in revised form 1 June 2016

Accepted 7 June 2016

Available online 7 June 2016

### Keywords:

Photocatalysis

Sulfur-doped TiO<sub>2</sub>

Visible light

Dimethyl sulfide

Reaction pathways

## ABSTRACT

Sulfur-doped TiO<sub>2</sub> prepared by a sol-gel method to degrade dimethyl sulfide (DMS) under visible light irradiation was investigated. The degradation reactions of DMS were performed under various operation conditions. The results indicate that S-doped TiO<sub>2</sub> photocatalysts are mainly nano-size with an anatase-phase structure. Relative humidity and inlet DMS concentration significantly influence the DMS conversion and mineralization. Langmuir-Hinshelwood kinetic models have been used in the analysis of the experimental data obtained. The main oxidation products of DMS photodegradation are SO<sub>2</sub>, CO<sub>2</sub>, DMDS, DMSO, DMSO<sub>2</sub>, CO, and MSA. Two possible mechanisms have been developed for photodegradation of DMS in a dry and a humid environment.

© 2016 Elsevier B.V. All rights reserved.

## 1. Introduction

Reduced sulfur compounds (RSCs) emissions from kraft pulp-milling mills, chemical plants, and livestock production have been serious phenomena [1]. Many of the emitted species are toxic, harmful and/or objectionable. Dimethyl sulfide (DMS) is one of typical odorous volatile organic sulfur compounds (VOSC) from photoresist processes of photoelectric industry, anaerobic wastewater treatment plants, composting plants, and rendering plants [2]. DMS has a specific smell like rotten cabbage and a very low odor threshold value (OTV) of 0.6–40 ppb [3,4]. The anthropogenic source can easily result in local concentrations strongly exceeding OTV [5]. Repeated exposure to odorous pollution can cause chronic respiratory and cardiovascular diseases [6]. Eliminating pollutant emissions is achievable to improve the quality of life for people living near paper mills or oil refineries [7].

Photocatalytic oxidation (PCO) using TiO<sub>2</sub> has recently received considerable attention for VOCs removal due to its cost-effective technology, non-toxicity, fast oxidation rate, and chemical stability [8]. However, the wide band gap of TiO<sub>2</sub> (3.2 eV for anatase), which is excited by photons with wavelengths shorter than 385 nm for photocatalytic activity, limits its application and photoreaction rates under visible light [9,10]. Many previous studies have

been investigated to narrow the band gap of TiO<sub>2</sub> and shift its light absorption spectrum into lower energy region [10]. Among them, band-gap modification of TiO<sub>2</sub> through nonmetal doping is considered as one of the most efficient methods to extend the absorption wavelength into visible light region [11]. Recent literatures indicated that sulfur is considered one of the most efficiently non-metal ions [12,13]. The mixing of the sulfur 3p states with oxygen 2p states was found to contribute to an increased width of the valence band, resulting in the defect states in the band gap [14]. The types of light sources used generally in photocatalytic studies and applications include UV lamp, Xe arc lamp, fluorescent lamp, and Hg-Xe lamp [15]. However, these traditional light sources are limited by shortcomings related to sustainability and the environment [6]. The development of light emitting diodes (LED) has increasingly attracted the attention of academic and industry researchers in recent years. LED technologies are known for its long lifetime, flexible configuration, small carbon footprint, and high energy efficiency [6,16].

Some studies indicated that the reactions by the PCO processes did not completely oxidize organics to CO<sub>2</sub> and H<sub>2</sub>O in many cases [17,18]. The reaction by-products of the photocatalytic system can be more toxic than the parent VOC, and those by-products may result hazardous to the human body. In this study, the characteristics of sulfur doped TiO<sub>2</sub>, photodegradation and mineralization of DMS, and kinetics of the reaction have been investigated under visible LED light irradiation. Besides, it was intended to gain insight

\* Corresponding author.

E-mail address: [chuhsin@mail.ncku.edu.tw](mailto:chuhsin@mail.ncku.edu.tw) (H. Chu).

into the reaction products, byproducts, and pathway for DMS photooxidation under visible light.

## 2. Experimental

### 2.1. Photocatalyst preparation

Sulfur-doped TiO<sub>2</sub> was prepared by the hydrolysis of titanium tetra-isopropoxide (TTIP) and thiourea (CH<sub>4</sub>N<sub>2</sub>S). In the preparation process of Ti-precursor sol, TTIP (30 mL) was mixed with absolute ethanol (45 mL). Then the mixture was slowly added into deionized water (360 mL) at room temperature during continuous stirring. After mixture was stirred for 30 min, nitric acid (65 wt%) was slowly added dropwise into the mixture. The pH of the sol was adjusted at 2 and further stirred until the gel formed at 70 °C on a heating plate. The final solution was stirred continuously until the liquid totally evaporated in a water bath at 70 °C for 8 h, and then the residual was calcined at 500 °C for 3 h in air. In the preparation of S/TiO<sub>2</sub>, the pre-determined amounts of thiourea (CH<sub>4</sub>N<sub>2</sub>S) were dissolved in 360 mL de-ionized water first, and the subsequent processes were the same as the method described above. Photo-catalysts prepared as S-doped TiO<sub>2</sub> were denoted as S<sub>x</sub>/TiO<sub>2</sub> (x = S/Ti molar ratio). In our previous study [19], the effect of sulfur doping ratio on DMS degradation by various photocatalysts was carried out in a laboratory-scale continuous reactor. Although the photocatalytic activity enhanced with increasing sulfur content, lower photocatalytic activities were obtained when sulfur contents were above 5 mol%. Therefore, S<sub>0.05</sub>/TiO<sub>2</sub> was chosen to further investigate various aspects of DMS photodegradation in this study.

### 2.2. Photocatalyst characterization

Transmission electron microscopy (TEM) images of nano-scale samples were obtained on a TEM instrument (JEM-2100F, Jeol Co. Ltd.). HRTEM analysis was performed on a carbon coated copper grids at an accelerating voltage of 200 kV. The samples were ultrasonically dispersed in ethanol to form dilute suspensions and then dropped a few droplets on carbon-coated copper grids. After that the samples were dried at room in air for 12 h before loading into the TEM. Image processing and evaluation of interplanar distance were performed using the DigitalMicrograph software (Gatan Inc., Pleasanton, CA, USA). Fourier transform infrared (FT-IR) spectra (Model Spectrum One, PerkinElmer) were recorded using KBr pellets. Diffuse reflectance FTIR spectra of outlet gases were recorded in the scan range from 4000 to 700 cm<sup>-1</sup> at a resolution of 4 cm<sup>-1</sup> with the use of Time Base 2.0 software.

### 2.3. Photocatalytic activity measurements

Gas phase photocatalysis was conducted in continuous flow mode using an annular flow-through reactor of about 340 mL volume, constructed with stainless steel, a glass cylinder, quartz light window, and a cool-white LED lamp. The photocatalyst layer was prepared by spin-coating catalysts onto the internal glass tube surface. A 72 W cool-white LED lamp was used as the photon source with light wavelength of 420–650 nm. The desired reaction gases were prepared by means of mixing air and DMS. The DMS contaminated stream was generated by an automated syringe pump at the preset injection rate. The reaction gas was humidified by passing a fraction of the humidified air through a gas-washing bottle, and the water content was determined based on the air flow rate and the ambient temperature. DMS concentration was measured on-line by a gas chromatography–mass spectroscopy (Shimadzu, GCMS-QP2010) equipped with a DB-1MS column. The concentration of CO<sub>2</sub> in the exhausted gas streams was continuously measured by a CO<sub>2</sub> analyzer (Molecular Analytics AGM 4000 Gas Analyzer). The

**Table 1**

Crystal phase, crystallite size, and lattice parameters of various photocatalysts.

Sample	Crystal phase	Crystallite size	Lattice parameters		
	Anatase (%)	d <sub>A</sub> (nm)	a (Å)	c (Å)	c/a
TiO <sub>2</sub>	100	16.0	3.774	9.448	2.504
S <sub>0.01</sub> /TiO <sub>2</sub>	100	16.0	3.774	9.534	2.526
S <sub>0.05</sub> /TiO <sub>2</sub>	100	11.1	3.775	9.548	2.529
S <sub>0.10</sub> /TiO <sub>2</sub>	100	11.4	3.778	9.546	2.527
S <sub>0.15</sub> /TiO <sub>2</sub>	100	11.8	3.775	9.457	2.505
S <sub>0.20</sub> /TiO <sub>2</sub>	100	13.1	3.774	9.436	2.500

byproducts and products were analyzed using an on-line FTIR spectrophotometer (Model Spectrum One, PerkinElmer) in the spectral range of 4000–700 cm<sup>-1</sup>. The conversion of DMS was calculated from the difference between the inlet and outlet DMS concentrations by the following equation:

$$\text{Conversion (\%)} = \left( \frac{C_{in} - C_{out}}{C_{in}} \right) \times 100 \quad (1)$$

where C<sub>in</sub> and C<sub>out</sub> are the inlet and outlet concentrations of DMS (ppm), respectively. The degree of DMS mineralization can be denoted as:

$$\text{Mineralization (\%)} = \frac{[\text{CO}_2]_{\text{measured}}}{[\text{CO}_2]_{\text{theoretical}}} \times 100 \quad (2)$$

$$[\text{CO}_2]_{\text{theoretical}} = \frac{2 \times \text{conversion (\%)} \times C_{in}}{100} \quad (3)$$

where [CO<sub>2</sub>]<sub>measured</sub> and [CO<sub>2</sub>]<sub>theoretical</sub> are the carbon dioxide concentrations measured (CO<sub>2</sub>) and transformed from DMS conversion, respectively.

## 3. Results and discussion

### 3.1. XRD analysis

The crystal phases, Scherrer crystallite sizes, and lattice parameter of various photocatalysts are given in Table 1. All of photocatalysts contain only anatase crystals (JCPDS Card No. 21-1272) and they have not undergone transition to rutile phase. The crystallite sizes of all sulfur doped TiO<sub>2</sub> are smaller than that of bare TiO<sub>2</sub> (16 nm), which indicates that S atoms have been incorporated into the lattice of TiO<sub>2</sub>. The phenomena are demonstrated by a change in the values of the lattice parameters, especially for S<sub>0.05</sub>/TiO<sub>2</sub>. There are no significant changes in lattice parameter 'a', but lattice parameter in 'c' obviously varies. The result is ascribed to the occurrence of a slight lattice distortion in the crystal structure, which causes the expansion of unit cell volume. For S-doped TiO<sub>2</sub>, the ionic radius of S<sup>6+</sup> in coordination IV is 0.12 Å, which can substitute Ti<sup>4+</sup> ions (Ti<sup>4+</sup> radius is 0.68 Å) in the TiO<sub>2</sub> crystal lattice. The radius of S<sup>2-</sup> (1.7 Å) is larger than that of O<sup>2-</sup> (1.22 Å), so the sites of O atoms are difficultly to be substituted with S<sup>2-</sup> in the anatase TiO<sub>2</sub> matrix [20]. In addition, the existing Ti–O bond energy (672.4 kJ mol<sup>-1</sup>) is larger than Ti–S bond (418 kJ mol<sup>-1</sup>) [21]. Therefore, sulfur substitution for oxygen in TiO<sub>2</sub> is energetically not favorable [8]. Thus, S<sup>6+</sup> cations substituted for the lattices titanium (Ti<sup>4+</sup>) is more favorable than the substitution of O<sup>2-</sup> by S<sup>2-</sup>, and causes the formation of Ti–O–S bond in TiO<sub>2</sub> structure.

### 3.2. TEM analysis

The HRTEM images of bare TiO<sub>2</sub> and S<sub>0.05</sub>/TiO<sub>2</sub> are shown in Fig. 1. The average crystallite size of TiO<sub>2</sub> is between 16 and 18 nm, and the size of the S<sub>0.05</sub>/TiO<sub>2</sub> is about 10–11 nm. The sulfur incorporation decreases the mean particle size, which implies the occurrence of a slight lattice distortion in the crystal structure. The

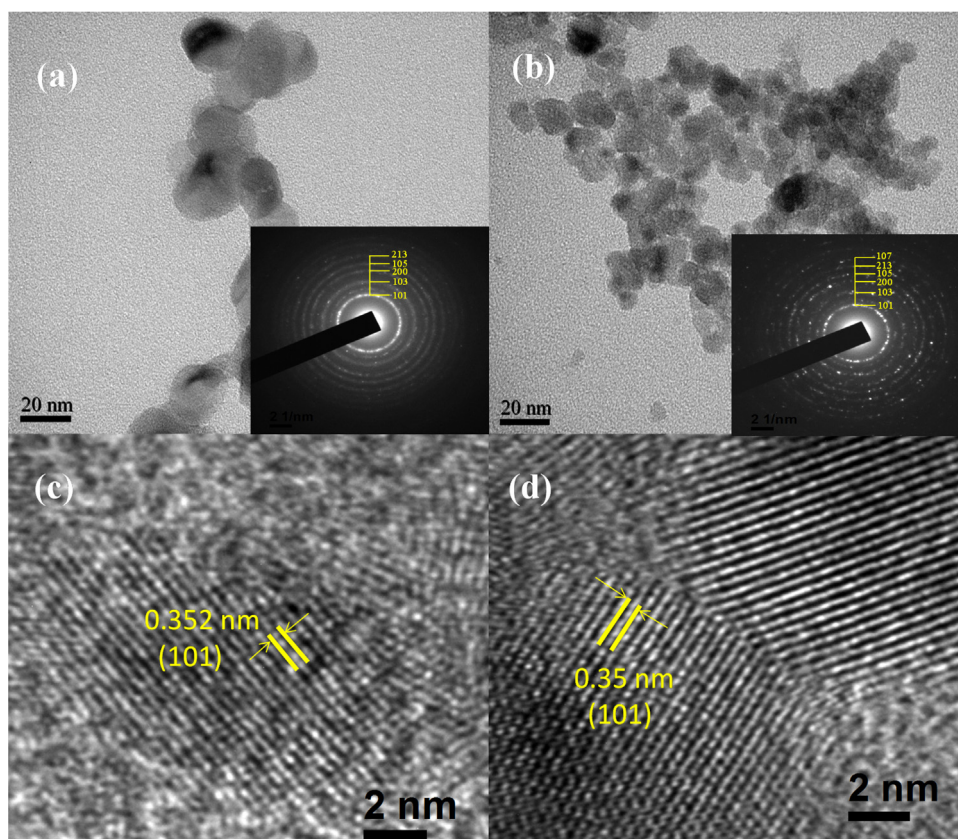


Fig. 1. TEM images of (a)  $\text{TiO}_2$  and (b)  $\text{S}_{0.05}/\text{TiO}_2$ , and HRTEM images of (c)  $\text{TiO}_2$  and (d) the  $\text{S}_{0.05}/\text{TiO}_2$ .

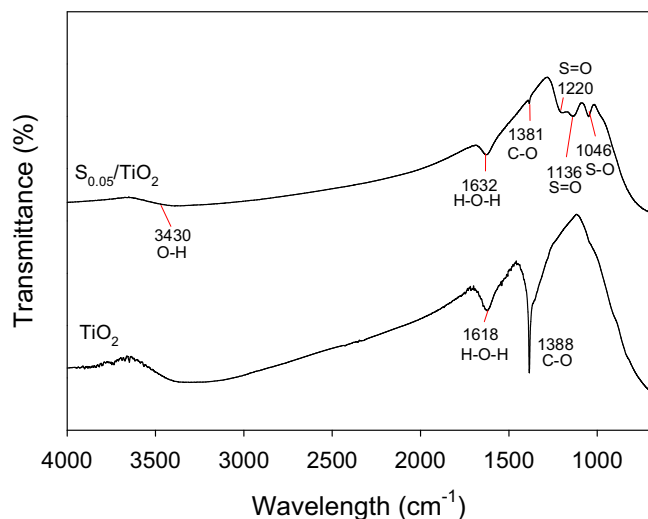


Fig. 2. FTIR spectra of the photocatalysts:  $\text{TiO}_2$  and  $\text{S}_{0.05}/\text{TiO}_2$ .

selected area electron diffraction SAED patterns are presented in the insets of Fig. 1a and b. The corresponding SAED patterns clearly reveal the diffraction spots from the (101), (103), (200), and (105) anatase reflections. From Fig. 1c and d, the interplanar distances are 0.352 and 0.35 nm in bare  $\text{TiO}_2$  and  $\text{S}_{0.05}/\text{TiO}_2$ , respectively, which match with the (101) planes of anatase  $\text{TiO}_2$ .

### 3.3. FTIR analysis

FTIR spectra of undoped and S-doped  $\text{TiO}_2$  are presented in Fig. 2 to further confirm the XRD analysis. For the case of  $\text{TiO}_2$ , the

broad absorbance between 3,930 and 3400  $\text{cm}^{-1}$  can be assigned to O–H stretching vibrations. The absorption peaks located at 1618 and 1632  $\text{cm}^{-1}$  for  $\text{TiO}_2$  and  $\text{S}_{0.05}/\text{TiO}_2$ , respectively, indicate the adsorption of water molecules (H–O–H bending vibrations) exists on the surface of the gel. The absorption spectrum of C–O is located at 1330–1390  $\text{cm}^{-1}$ . For the case of  $\text{S}_{0.05}/\text{TiO}_2$ , a new peak appears at 1046  $\text{cm}^{-1}$ , which is ascribed to the S–O asymmetric stretch. The two peaks corresponding to 1136 and 1220  $\text{cm}^{-1}$  are the characteristic asymmetric and symmetric stretch absorption peaks of S=O, respectively [22]. These characteristic peaks are linked to the presence of bidentate  $\text{SO}_4^{2-}$  coordinated to  $\text{Ti}^{4+}$ . The result implies the formation of Ti–O–S bonds [23,24]. The FTIR results confirm that  $\text{S}^{6+}$  with a radius of 0.12 Å can penetrate into the  $\text{TiO}_2$  structure ( $\text{Ti}^{4+}$  radius is 0.68 Å). This indicates that the mixing of the S 3p state with the valence band contributes to the band-gap narrowing to further extend the absorption wavelength into the visible light region [25].

### 3.4. Operating parameters in photo-degradation processes

A series of experiments was conducted to evaluate the influence of three important parameters (residence time, inlet gas concentration and relative humidity (RH)) on the conversion and mineralization of DMS. All experiments were performed in duplicate and data were recorded under steady-state conditions (A typical run required 60 min to 150 min to reach a steady state after the experiment started).

The catalytic activity of the photocatalyst  $\text{S}_{0.05}/\text{TiO}_2$  was investigated in DMS degradation in the residence time range of 35–180 s, and the results are shown in Fig. 3a. The conversion of DMS increases from 84.8 to 97.8% when the residence time increases from 35 to 180 s. The phenomenon is ascribed to a longer con-

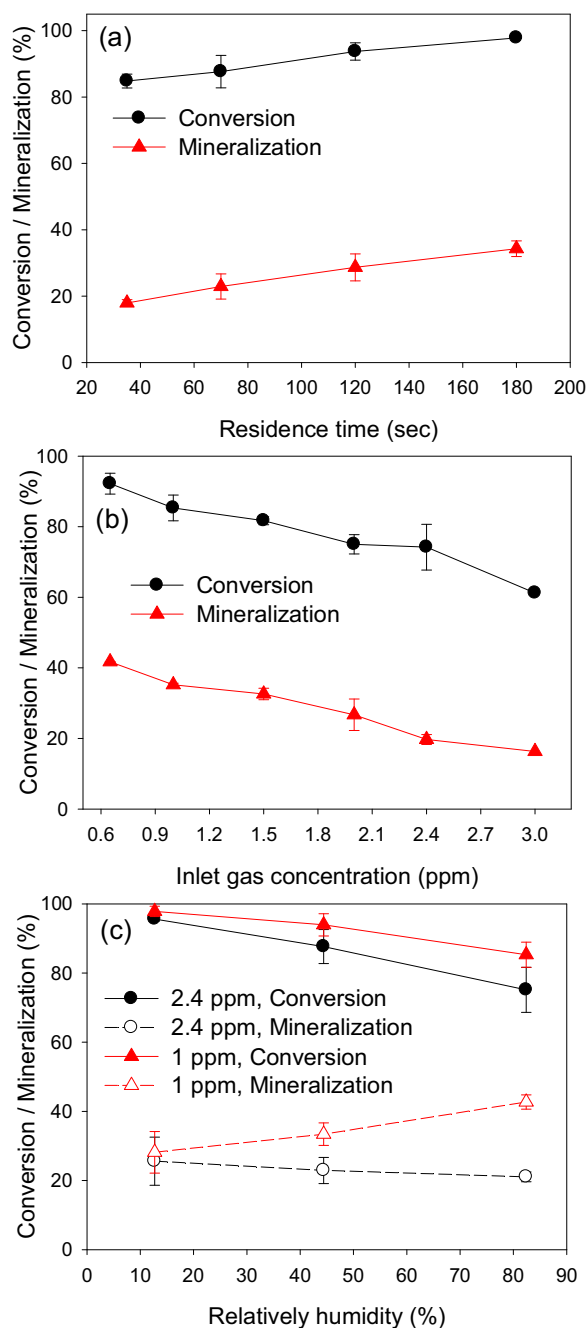


**Fig. 3.** Effect of (a) residence time ( $[O_2]=21\%$ ,  $[DMS]=1.7\text{--}2.8$  ppm,  $[RH]=44.5\%$ , Temp. =  $45^\circ\text{C}$ ), (b) inlet gas concentration ( $[O_2]=21\%$ ,  $[RH]=82.6\%$ , residence time = 70 s, Temp. =  $45^\circ\text{C}$ ), and (c) relative humidity ( $[O_2]=21\%$ ,  $[DMS]=1\text{--}2.4$  ppm, residence time = 70 s, Temp. =  $45^\circ\text{C}$ ) on the photo-degradation of DMS by  $S_{0.05}/TiO_2$ .

tact time between the photocatalyst and the pollutants [26,27]. At a longer residence time, a greater collision frequency occurs between the hydroxyl radicals and the pollutants [28]. Therefore, the conversion and carbon mineralization of DMS increases.

The effect of inlet gas concentration on DMS conversion and carbon mineralization are shown in Fig. 3b. The inlet concentration of DMS was controlled from 0.65 to 3 ppm. The higher concentration of DMS means that DMS normally has a greater chance of collision with hydroxyl radicals hence the greater is the yield of carbon dioxide. However, the conversion and carbon mineralization decrease with an increase of inlet concentration. When inlet DMS concentration was set at 0.65 ppm, the highest conversion and carbon mineralization are obtained although the reaction rate

may be lower. The result indicates that the photocatalytic oxidation is limited by the number of active sites on the catalyst surface. The competitive adsorption can occur between the byproducts and contaminant molecules, and the active sites of the photocatalyst are covered by byproducts at higher concentrations. The amount of formation of byproducts and products are higher at higher inlet gas concentration, and therefore, there is insufficient time to diffuse these byproducts and products into non-irradiated parts of photocatalyst and they occupy active sites.

The rate of formation of products is faster at higher inlet gas concentration, and therefore, there is insufficient time to diffuse these products into non-irradiated parts of photocatalyst and they occupy active sites.

The influence of relative humidity on DMS conversion and carbon mineralization was conducted at various RH levels from 12.7 to 82.4%, which is shown in Fig. 3c. DMS inlet concentration was set at 1 or 2.4 ppm. The result shows that at low DMS level the PCO oxidation has a better conversion and carbon mineralization than that obtained at higher concentration. Besides, the conversion decreases with an increase in relative humidity under two-level inlet DMS concentrations. However, the opposite result was obtained for carbon mineralization as a function of RH under two-level inlet DMS concentrations. The results of conversion and mineralization as a function of RH are significantly different. The carbon mineralization is only ranged from 23 to 41%, which indicates carbon mineralization is not complete and reaction intermediates are not totally oxidized. The phenomenon is attributed to the two mechanisms of water vapor on photocatalytic oxidation: (i) the photocatalytic degradation of VOCs increases due to the formation of hydroxyl radicals and (ii) the presence of excess water vapor reduce the reactivity due to the competitive adsorption of water vapor and DMS on the active sites of the photocatalysts.

The presence of water vapor enhances the degradation of intermediates toward carbon mineralization at low DMS level. The result indicates that the PCO not only relies on the number of active sites but also the residence time at low DMS concentration. In contrary, at high DMS concentration, the photoactivity and mineralization are limited significantly by the number of active sites on photocatalysts surface and competitive adsorption is observed among water vapor, byproducts and DMS with increasing relative humidity. More water molecules occupy the active sites as time goes on, which impedes the decomposition of DMS and carbon mineralization. The result also demonstrates photocatalytic conversion and carbon mineralization are correlated to photocatalyst conditions and reaction mechanisms.

### 3.5. Kinetics of DMS photooxidation

The Langmuir–Hinshelwood (L–H) kinetic model has been widely used in the gas–solid phase reaction for heterogeneous photocatalysis [29,30]. According to the effect of the molar doping ratio,  $S_{0.05}/TiO_2$  was chosen to investigate the reaction kinetics of photocatalysis. The experimental photocatalytic oxidation rate can be deduced from the mass balance for a plug flow reactor, which can be presented as Eq. (4):

$$-r = \frac{F}{V} X_i = \frac{F}{V} \left( \frac{C_{in} - C_{out}}{C_{in}} \right) \quad (4)$$

where  $r$  is the reaction rate of DMS ( $\text{mol cm}^{-3} \text{ min}^{-1}$ ),  $C_{in}$  and  $C_{out}$  are the DMS inlet and outlet concentrations ( $\text{mol cm}^{-3}$ ), respectively,  $V$  is the volume of the reactor (340 mL),  $F$  is the gas flow rate ( $\text{mL min}^{-1}$ ).

Seven models were used based on various assumptions as presented in Table 2 [27,31–33]. A non-linear least square regression analysis was used to evaluate the goodness of fit and determine the values of the rate constants and the adsorption equilibrium

**Table 2**

The Langmuir-Hinshelwood models of PCO reaction [27,31–33].

Model	Kinetics rate expression	Assumption
1	$-r = k \times \frac{K_A C_A}{1 + K_A C_A}$	Reaction of VOCs adsorbed on catalyst surface but water does not take part in the reaction.
2	$-r = k \times \frac{K_A C_A K_W C_W}{1 + K_A C_A + K_W C_W}$	Reaction of VOCs adsorbed on catalyst surface and react with water.
3	$-r = k \times \frac{K_A C_A}{1 + K_A C_A + K_W C_W}$	VOCs and water adsorbed on catalyst surface but water does not take part in the reaction.
4	$-r = k \times \frac{K_A C_A K_W C_W}{1 + K_A C_A + K_W C_W}$	Reaction of VOCs and water adsorbed on catalyst surface.
5	$-r = k \times \frac{K_A C_A}{1 + K_A C_A} \times \frac{K_W C_W}{1 + K_W C_W}$	Reaction of VOCs and water adsorbed on different active sites.
6	$-r = k \times \frac{K_A C_A K_W C_W}{1 + K_W C_W}$	Reaction of water adsorbed on catalyst surface and gas-phase VOCs.
7	$-r = k \times \frac{(K_A C_A K_W C_W)^{1/2}}{[1 + (K_A C_A)^{1/2} + (K_W C_W)^{1/2}]^2}$	Reaction of VOCs and water dissociatively adsorbed on catalyst surface.

Symbol description:  $K_A$  and  $K_W$  are the adsorption equilibrium constant of DMS and water vapor ( $\text{cm}^3 \text{mol}^{-1}$ ), respectively.  $k$  is reaction rate constant ( $\text{mol cm}^{-3} \text{min}^{-1}$ ).  $C_A$  and  $C_W$  are the concentrations of DMS and water vapor ( $\text{mol cm}^{-3}$ ), respectively.

constants. The experimental data was fitted using the Polymath 6.10 software. The program uses the Levenberg-Marquardt (LM) algorithm to estimate the constants of various models [27]:

$$\text{RSS} = \sum (\text{R}_{\text{pred}} - \text{R}_{\text{exper}})^2 \quad (5)$$

where RSS is the residual sum of squares,  $\text{R}_{\text{pred}}$  is the model predicted rate, and  $\text{R}_{\text{exper}}$  is the experimental measured rate.

The regression results of  $k$ ,  $K_A$ , and  $K_W$  for various models by the polymath software are listed in Table 3. The value of  $R^2$  is used to determine the overall goodness of fit of the nonlinear model. The R-squared values in models 4 and 7 are higher than 0.9 for various temperatures. Besides, their adsorption equilibrium constants of DMS ( $K_A$ ) are larger than the adsorption equilibrium constants of water vapor ( $K_W$ ), and the adsorption equilibrium constants of  $K_A$  and  $K_W$  decrease with increasing temperature. The result indicates DMS is adsorbed more easily than water on the photocatalyst surface, and it is corresponding to the effect of relative humidity on DMS conversion and carbon mineralization. When the photodegradation of DMS was performed at high-level humidity, DMS was preferentially adsorbed onto the active sites of photocatalyst. There is competitive adsorption of DMS and water for the active sites of the photocatalyst, leading to sorption of water molecules at a less active site, therefore, water vapor would not dissociate to hydroxyl radicals to react with DMS. In contrast, there are extra active sites

to create hydroxyl radicals to react with DMS and byproduct at the low-level humidity.

The fittings of the model predicted reaction rate values versus the experimentally measured values are presented in Fig. 4. Fig. 4a shows the experimental data obtained with various inlet DMS concentrations and temperatures are in good accordance with models predicted values. The effect of temperature in the reaction rate constant was determined by the Arrhenius equation, expressed as follows:

$$k = k' \exp \left( -\frac{E_a}{RT} \right) \quad (6)$$

where  $k'$  is the (temperature-independence) rate constant ( $\text{mol cm}^{-3} \text{min}^{-1}$ ),  $E_a$  is the activation energy ( $\text{kJ mol}^{-1}$ ),  $T$  is the temperature (K), and  $R$  is the gas constant ( $8.31 \times 10^{-3} \text{ kJ mol}^{-1} \text{K}^{-1}$ ).

The adsorption equilibrium constant can be modified to include a temperature dependence in the rate equation, the following assumptions were made: (i) the temperature-dependent of the Langmuir adsorption constant can be used to determine the monolayer adsorption on a homogeneous surface and (ii) the rate constant exhibits a temperature dependence that follows the

**Table 3**

Rate and adsorption equilibrium constants for each model in the presence of water.

Model	Temp. (°C)	$k$ ( $\text{mol cm}^{-3} \text{min}^{-1}$ )	$K_A$ ( $\text{cm}^3 \text{mol}^{-1}$ )	$K_W$ ( $\text{cm}^3 \text{mol}^{-1}$ )	RSS	$R^2$
1	35	$8.93 \times 10^{-1}$	$5.76 \times 10^{-1}$	–	$3.63 \times 10^{-22}$	0.76
	45	$9.73 \times 10^{-1}$	$6.27 \times 10^{-1}$	–	$1.96 \times 10^{-21}$	0.13
	55	1.24	$8.00 \times 10^{-1}$	–	$1.58 \times 10^{-21}$	0.61
2	35	1.56	13.5	$1.36 \times 10^4$	$6.60 \times 10^{-21}$	0.00
	45	1.48	12.7	$1.29 \times 10^4$	$5.90 \times 10^{-21}$	0.00
	55	1.40	12.1	$1.22 \times 10^4$	$1.49 \times 10^8$	0.00
3	35	$3.80 \times 10^{-4}$	$1.66 \times 10^3$	$2.30 \times 10^5$	$8.04 \times 10^{-23}$	0.95
	45	$3.50 \times 10^{-4}$	$1.52 \times 10^3$	$-6.71 \times 10^4$	$1.76 \times 10^{-21}$	0.21
	55	$5.38 \times 10^{-4}$	$2.34 \times 10^3$	$1.00 \times 10^5$	$2.49 \times 10^{-22}$	0.94
4	35	$2.29 \times 10^{-10}$	$6.42 \times 10^{12}$	$1.22 \times 10^9$	$6.17 \times 10^{-23}$	0.93
	45	$3.22 \times 10^{-10}$	$3.30 \times 10^{12}$	$3.77 \times 10^8$	$7.52 \times 10^{-23}$	0.94
	55	$4.35 \times 10^{-10}$	$1.58 \times 10^{12}$	$1.13 \times 10^8$	$9.21 \times 10^{-23}$	0.96
5	35	$8.39 \times 10^{-3}$	52.7	$1.81 \times 10^{15}$	$2.18 \times 10^{-22}$	0.76
	45	$1.06 \times 10^{-3}$	$6.28 \times 10^2$	$1.98 \times 10^{16}$	$3.68 \times 10^{-22}$	0.71
	55	$5.73 \times 10^{-2}$	14.4	$3.24 \times 10^{15}$	$1.30 \times 10^{-21}$	0.45
6	35	$3.39 \times 10^2$	3.26	$2.60 \times 10^2$	$2.67 \times 10^{-21}$	0.00
	45	$3.19 \times 10^2$	3.06	$2.49 \times 10^2$	$5.51 \times 10^{-21}$	0.00
	55	$2.90 \times 10^2$	2.79	$2.54 \times 10^2$	$1.03 \times 10^{-20}$	0.00
7	35	$7.70 \times 10^{-9}$	$9.42 \times 10^6$	$7.21 \times 10^6$	$2.77 \times 10^{-23}$	0.97
	45	$1.19 \times 10^{-8}$	$8.07 \times 10^6$	$4.58 \times 10^6$	$1.35 \times 10^{-23}$	0.99
	55	$2.16 \times 10^{-8}$	$4.63 \times 10^6$	$3.10 \times 10^6$	$4.97 \times 10^{-23}$	0.98

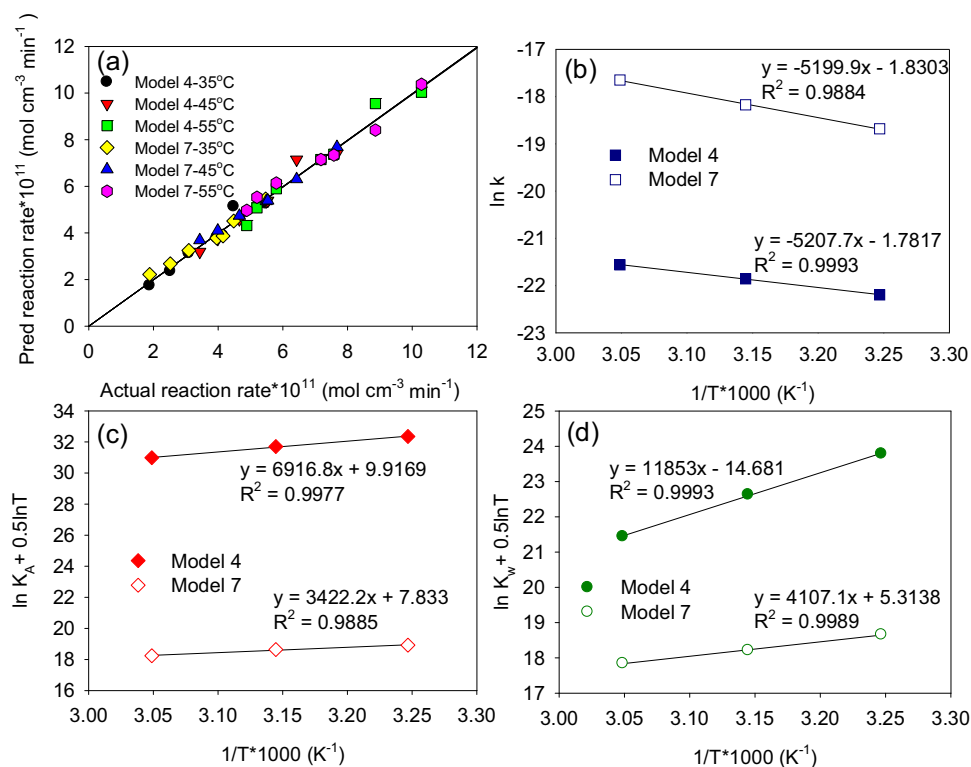


**Fig. 4.** (a) L–H model predicted reaction rate versus the experimental data, (b) Arrhenius equation fitting, (c) adsorption equilibrium constant of DMS, and (d) adsorption equilibrium constant of water vapor.

**Table 4**

The reaction rate constants and adsorption equilibrium constants of modified Langmuir–Hinshelwood models for Eqs. (4) and (7).

Parameters	Units	Model 4	Model 7
$k'$	$\text{mol cm}^{-3} \text{min}^{-1}$	$8.56 \times 10^{-6}$	$1.73 \times 10^{-1}$
$K_A'$	$\text{K}^{1/2} \text{cm}^3 \text{mol}^{-1}$	$2.03 \times 10^4$	$2.52 \times 10^3$
$K_W'$	$\text{K}^{1/2} \text{cm}^3 \text{mol}^{-1}$	$4.21 \times 10^{-7}$	$2.03 \times 10^2$
$E_a$	$\text{kJ mol}^{-1}$	27.0	41.8
$\Delta H_A$	$\text{kJ mol}^{-1}$	−57.5	−28.5
$\Delta H_W$	$\text{kJ mol}^{-1}$	−98.6	−34.2

Arrhenius law [34]. The temperature dependent adsorption constant is determined by the following equation:

$$K = K' \frac{\exp(-\Delta H/RT)}{\sqrt{T}} \quad (7)$$

where  $K$  ( $\text{cm}^3 \text{mol}^{-1}$ ) is the adsorption equilibrium constant,  $K'$  ( $\text{K}^{1/2} \text{cm}^3 \text{mol}^{-1}$ ) is the temperature-independence adsorption equilibrium constant, and  $\Delta H$  ( $\text{kJ mol}^{-1}$ ) is the enthalpy change of reactants. Eqs. (6) and (7) can be substituted into models 4 and 7 to describe temperature-dependent simulation model, and the apparent activation energy of photocatalytic process and the reaction enthalpy of DMS and water can be calculated.

The least-squares analysis was used to determine the optimized regression values, which are presented in Fig. 4b–d. Table 4 shows the reaction rate constants, adsorption equilibrium constants, apparent activation energy, and enthalpy of reactants. The activation energies of models 4 and 7 are 27.0 and 41.8  $\text{kJ mol}^{-1}$ , respectively. The values of enthalpy for DMS and physisorbed water in model 4 are −57.5 and −98.6  $\text{kJ mol}^{-1}$ , respectively. The enthalpies of DMS and physisorbed water are −28.5 and −34.2  $\text{kJ mol}^{-1}$ , respectively for model 7. A previous study indicated that the enthalpy of adsorption for physisorbed water on  $\text{TiO}_2$  was −51  $\text{kJ mol}^{-1}$  [35]. Vittadini et al. studied the binding energy of the molecular adsorption and dissociative adsorption of water on the

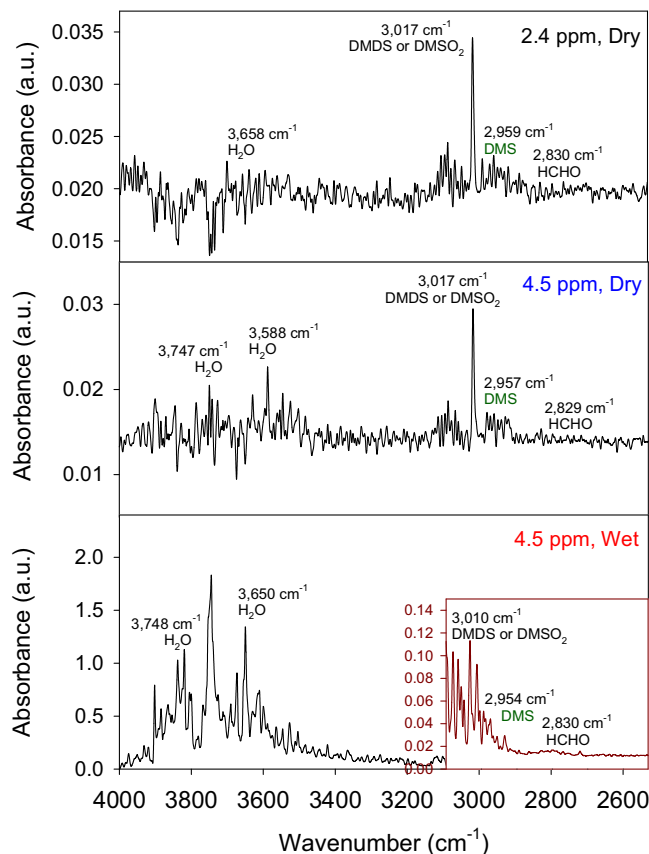


**Fig. 5.** FTIR spectra of byproducts and products of DMS photocatalysis in the wavenumbers of 4000–2530  $\text{cm}^{-1}$  (white LED light,  $[\text{DMS}] = 2.4\text{--}4.5$  ppm,  $\text{RH} = 0\text{--}82.6\%$ ,  $[\text{O}_2] = 21\%$ ,  $\text{Temp.} = 45^\circ\text{C}$ ).

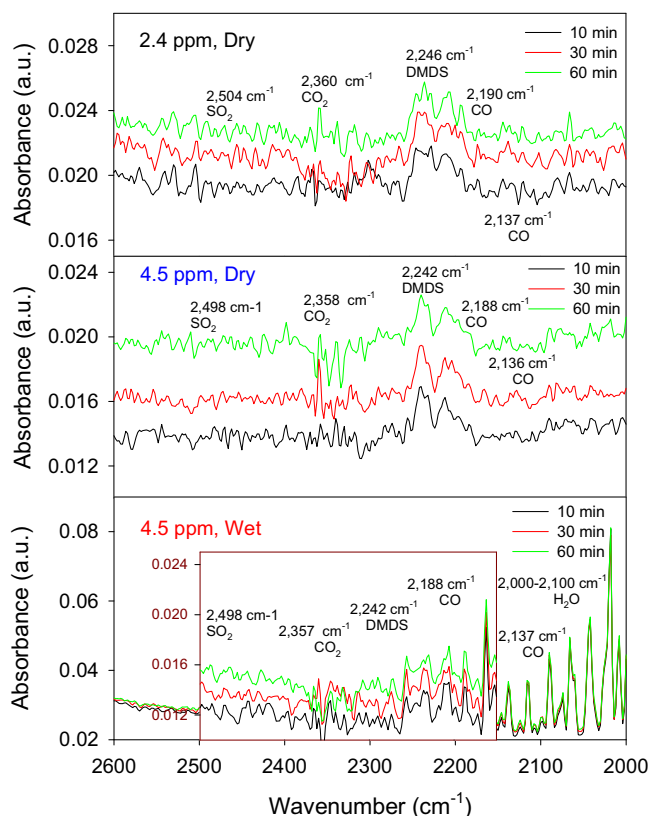


**Fig. 6.** FTIR spectra of byproducts and products of DMS photodegradation in the wavenumbers of 2600–2000  $\text{cm}^{-1}$  (white LED light,  $[\text{DMS}] = 2.4\text{--}4.5$  ppm,  $\text{RH} = 0\text{--}82.6\%$ ,  $[\text{O}_2] = 21\%$ ,  $\text{Temp.} = 45^\circ\text{C}$ ).

anatase (101) surface using density functional theory and reported an adsorption energy of 71.4 and 29.0  $\text{kJ mol}^{-1}$ , respectively [36]. The phenomena implied dissociative adsorption of water was more favorable than molecular adsorption on the anatase surface [36]. Based on the above information, it indicates that the interaction of water on  $\text{TiO}_2$  surface belongs to dissociative adsorption. Therefore, model 7 appears suitable for predicting the reaction rate in this study.

### 3.6. Photodegradation products and byproducts

In order to investigate byproducts and products of DMS photodegradation, a series of FTIR observations have been performed and the results are shown in Figs. 5–7. IR spectra were demonstrated with reference from the database [37]. According to above conversion results, the inlet DMS concentration and relative humidity were set at two levels ( $[\text{DMS}]_{\text{in}} = 2.4, 4.5$  ppm and dry = 0% RH, wet = 82.5% RH).

The absorptions peaks around 3500–3750 and 1600–1700  $\text{cm}^{-1}$  are attributed to  $\text{H}_2\text{O}$ , which is formed during the photocatalytic degradation of DMS or water vapor originally in a gas stream. The peaks intensity of water presents higher strength in a wet condition than in a dry condition. The scales of IR absorbance are magnified 16, 4.5, and 8.8 times in the corresponding insets for Figs. 5–7, respectively. In the dry condition, the absorption spectrum located at around 3017  $\text{cm}^{-1}$  is the characteristic peak of dimethyl disulfide (DMDS) or dimethyl sulfone ( $\text{DMSO}_2$ ). The absorption bands assigned at about 2957 (antisymmetric stretch of methyl group  $\text{CH}_3$ ,  $\nu_{\text{CH}_3}^{\text{as}}$ ) and 1306  $\text{cm}^{-1}$  (symmetric deformation of  $\text{CH}_3$ ,  $\delta_{\text{CH}_3}^{\text{s}}$ ) are attributed to DMS molecules [38]. The bands at about 2504 (overtone bands of  $\nu_{\text{S=O}}^{\text{as}}$ ) and 1357  $\text{cm}^{-1}$  ( $\nu_{\text{S=O}}^{\text{as}}$ ) are assigned to gaseous sulfur dioxide ( $\text{SO}_2$ ) [38]. The broad absorbance at about 2360  $\text{cm}^{-1}$

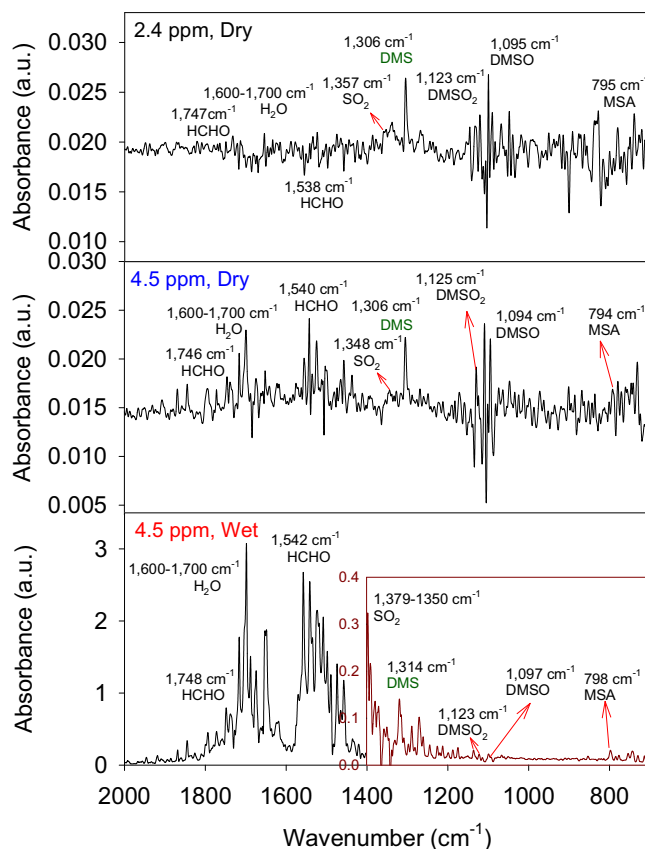
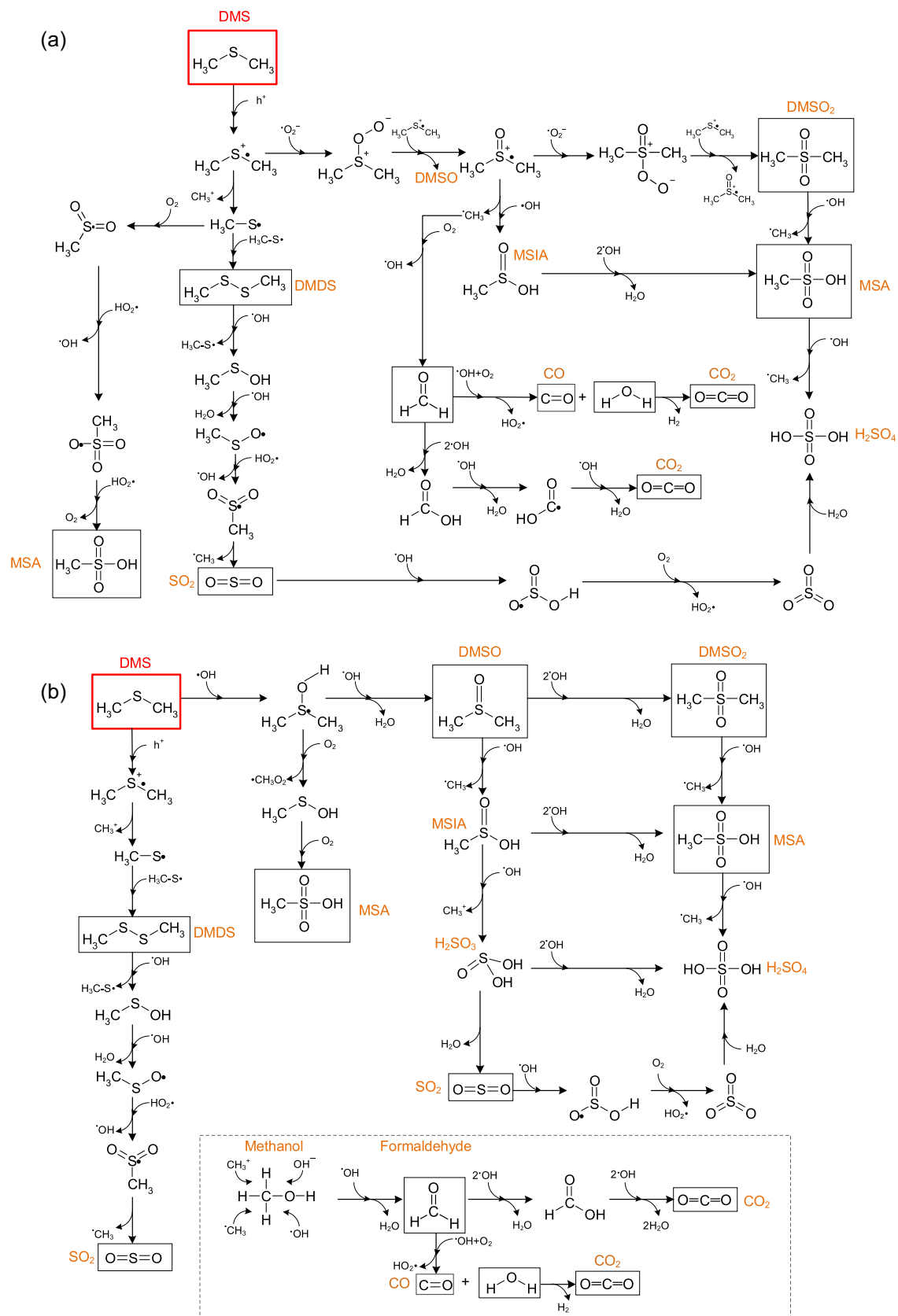


**Fig. 7.** FTIR spectra of byproducts and products of DMS photodegradation in the wavenumbers of 2000–700  $\text{cm}^{-1}$  (white LED light,  $[\text{DMS}] = 2.4\text{--}4.5$  ppm,  $\text{RH} = 0\text{--}82.6\%$ ,  $[\text{O}_2] = 21\%$ ,  $\text{Temp.} = 45^\circ\text{C}$ ).

can be assigned to carbon dioxide. The CO-molecule stretching vibrations are observed in the range between 2198 and 2137  $\text{cm}^{-1}$ . The absorption bands at about 1747 and 1540  $\text{cm}^{-1}$  are characterizing of formaldehyde (HCHO) [39]. The absorptions bands at about 1123, 1095 and 795  $\text{cm}^{-1}$  are assigned to  $\text{DMSO}_2$ , dimethyl sulfoxide (DMSO), and methanesulfonic acid (MSA), respectively [40]. It can be obtained that the absorbance intensities of species in the wet condition are stronger than that of the dry condition (Figs. 5–7). In the beginning, a significant amount of  $\text{CO}_2$  (peaks at 2350–2360  $\text{cm}^{-1}$ ) is produced in wet condition, and a small amount of  $\text{CO}_2$  and some  $\text{H}_2\text{O}$  are produced in the dry condition, as shown in Figs. 5 and 6. The result denotes hydroxyl radicals enhance the degradation of intermediates toward carbon mineralization and modify byproducts composition, which corresponds to the influence of relative humidity on DMS degradation (Section 3.3). As reaction time goes on the absorbance intensities of  $\text{CO}_2$  decreased, which is attributed to the competitive adsorption of the water and contaminant molecules at higher DMS concentration.

### 3.7. Reaction pathways

The decomposition of DMS occurs by attacking from superoxide or hydroxyl radicals, and its selectivity strongly depends on the reaction conditions. When a lamp is turned on, the production of photo-induced electrons and holes is achieved. The positively charged holes generate hydroxyl radicals ( $\cdot\text{OH}$ ) by reacting with adsorbed water, and then initiate the oxidation of the adsorbed organic compounds. In the reduction reaction, the negatively charged electrons react with adsorbed oxygen molecules to

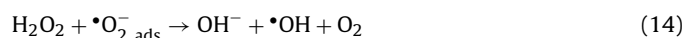


form superoxide radicals ( $\bullet\text{O}_2^-$ ). The reaction steps are listed in the following reactions:



Based on the FT-IR identification results,  $\text{SO}_2$ , DMSO,  $\text{DMSO}_2$ , DMDS, and MSA are the major photodegradation sulfur-containing products of gaseous DMS, and  $\text{CO}_2$ , CO, and  $\text{H}_2\text{O}$  are also presented in the gas phase. The degradation pathways of DMS are therefore proposed in (a) dry condition and (b) wet condition, as shown in Fig. 8.

In the case of dry condition, the absorption bands of  $\text{H}_2\text{O}$  are tiny, which imply the electron and oxygen play a key role in the photodegradation process.  $\text{O}_2$  molecules react with electrons to produce superoxide radicals ( $\bullet\text{O}_2^-$ ). There are two main reactions for the dry condition: S oxidation by superoxide radicals and C–S bond cleavage. The direct oxidation of DMS by  $h\nu$  forms dimethyl sulfinium radical ( $(\text{CH}_3)_2\text{S}^\bullet$ ), which is further oxidized by  $\bullet\text{O}_2^-$  radical to generate DMSO and  $\text{DMSO}_2$  [2,41]. The methyl radicals ( $\bullet\text{CH}_3$ ) is formed shortly through C–S bond cleavage in a dimethyl sulfoxonium radical ( $(\text{CH}_3)_2\text{SO}^\bullet$ ), and then is oxidized by  $\bullet\text{O}_2^-$  radical (molecular oxygen) to form formaldehyde (HCHO), carbon dioxide, carbon monoxide, and water [41]. The formation of hydroperoxyl radical ( $\text{HO}_2^\bullet$ ) and hydroxyl radicals ( $\bullet\text{OH}$ ) can be described according to the reactions given below [42]:



Methane sulfinic acid (MSIA,  $\text{CH}_3\text{SO}_2\text{H}$ ) is formed through C–S bond cleavage in a dimethyl sulfoxonium radical and  $\bullet\text{OH}$  radical attack. The  $\bullet\text{OH}$  radical attack also leads to the formation of MSA [38,40]. The dimethyl sulfinium radical ( $(\text{CH}_3)_2\text{S}^\bullet$ ) on further oxidation yields MSA and releases methyl cation ( $\text{CH}_3^+$ ). In addition, DMDS is produced through  $\text{CH}_3\text{S}^\bullet$  radical self-recombination in the direct splitting of the C–S bond [43,44]. Further oxidation by  $\bullet\text{OH}$  radical can result in the formation of  $\text{SO}_2$  [45].

Fig. 8b illustrates two potential reaction pathways in wet condition: S oxidation by  $\bullet\text{OH}$  radical and C–S bond cleavage. DMS molecule can be oxidized directly by  $\bullet\text{OH}$  radical to form DMSO,  $\text{DMSO}_2$ , MSA, and MSIA and release methyl radical in wet condition [38,44]. A further attack by  $\bullet\text{OH}$  radical, MSA and MSA can generate sulfur dioxide and sulfate, and release methyl radicals [46]. Another possible reaction pathway involves first forming dimethyl sulfinium radical, which is to split into a  $\text{CH}_3\text{S}^\bullet$  radical and a methyl cation. The dimerization of  $\text{CH}_3\text{S}^\bullet$  radicals causes the formation of DMDS and is oxidized by  $\bullet\text{OH}$  radical to form  $\text{SO}_2$ . This series of reactions causes the production of methyl radicals, methyl cations,  $\bullet\text{OH}$ , and  $\text{OH}^-$ , which can form methanol. The oxidation of methanol by  $\bullet\text{OH}$  radical in the photodecomposition leads to the formation of formaldehyde ( $\text{CH}_2\text{O}$ ), carbon monoxide (CO), and  $\text{CO}_2$ .

#### 4. Conclusion

In this study, the sulfur-doped  $\text{TiO}_2$  catalysts were successfully prepared by a sol-gel method. The  $\text{S}_{0.05}/\text{TiO}_2$  exhibits the best DMS decomposition rate. At low DMS concentration, PCO depends on the number of active sites and the residence time. In contrary, at high concentration level, the photoactivity and mineralization are the direct results of competitive adsorption of water and VOCs. The results show that conversion (%) and mineralization (%) of DMS

exhibit different trends as a function of DMS concentration and RH level. Kinetics study of photo-degradation of DMS over  $\text{S}_{0.05}/\text{TiO}_2$  shows that the Langmuir-Hinshelwood model is a feasible way to describe the photodecomposition of DMS. Kinetic analysis shows that the interaction of water on  $\text{TiO}_2$  surface belongs to dissociative adsorption. The degradation pathways of DMS have been presented in a dry and a humid environment, respectively. Superoxide radicals and  $\bullet\text{OH}$  radical are considered the key species for the dry and wet reaction process, respectively.

#### Acknowledgement

This study was funded in part by the National Science Council, Republic of China, under grant NSC 105-3113-E-006-004.

#### References

- [1] K.C. Soni, S. Chandra Shekar, B. Singh, T. Gopi, J. Colloid Interface Sci. 446 (2015) 226–236.
- [2] C. Cantau, S. Larribau, T. Pigot, M. Simon, M.T. Maurette, S. Lacombe, Catal. Today 122 (2007) 27–38.
- [3] J.M. de Zwart, J.G. Kuenen, Biodegradation 3 (1992) 37–59.
- [4] D. Glindemann, J. Novak, J. Witherspoon, Environ. Sci. Technol. 40 (2006) 202–207.
- [5] E. Smet, P. Lens, H.V. Langenhove, Crit. Rev. Environ. Sci. Technol. 28 (1998) 89–117.
- [6] Z. Wang, J. Liu, Y. Dai, W. Dong, S. Zhang, J. Chen, J. Hazard. Mater. 215–216 (2012) 25–31.
- [7] R.E.R. de Souza Lourenço, L.C. Passoni, M.C. Canela, J. Mol. Catal. A: Chem. 392 (2014) 284–289.
- [8] Y.H. Lin, T.K. Tseng, H. Chu, Appl. Catal. A: Gen. 469 (2014) 221–228.
- [9] Y. Niu, M. Xing, J. Zhang, B. Tian, Catal. Today 201 (2013) 159–166.
- [10] G. Zhang, Y.C. Zhang, M. Nadagouda, C. Han, K. O'Shea, S.M. El-Sheikh, A.A. Ismail, D.D. Dionysiou, Appl. Catal. B: Environ. 144 (2014) 614–621.
- [11] S.M. El-Sheikh, G. Zhang, H.M. El-Hosainy, A.A. Ismail, K.E. O'Shea, P. Falaras, A.G. Kontos, D.D. Dionysiou, J. Hazard. Mater. 280 (2014) 723–733.
- [12] Y.H. Lin, S.H. Chou, H. Chu, J. Nanopart. Res. 16 (2014) 1–12.
- [13] Z. Wang, X. Liu, W. Li, H. Wang, H. Li, Ceram. Int. 40 (2014) 8863–8867.
- [14] T. Umehayashi, T. Yamaki, S. Yamamoto, A. Miyashita, S. Tanaka, T. Sumita, K. Asai, J. Appl. Phys. 93 (2003) 5156–5160.
- [15] J. Zhao, X. Yang, Build. Environ. 38 (2003) 645–654.
- [16] D.P. Subagio, M. Srinivasan, M. Lim, T.T. Lim, Appl. Catal. B: Environ. 95 (2010) 414–422.
- [17] H. Ourrad, F. Thevenet, V. Gaudion, V. Riffault, Appl. Catal. B: Environ. 168 (2015) 183–194.
- [18] O. Debono, F. Thévenet, P. Gravejat, V. Hequet, C. Raillard, L. Le Coq, N. Locoge, J. Photochem. Photobiol. A: Chem. 258 (2013) 17–29.
- [19] M.C. Chen, Photocatalytic Degradation of Dimethyl Sulfide Under Visible Light with S-doped  $\text{TiO}_2$  Photocatalysts, Master Thesis, National Cheng Kung University, Taiwan, 2012, pp. 103–105.
- [20] J.C. Yu, W. Ho, J. Yu, H. Yip, P.K. Wong, J. Zhao, Environ. Sci. Technol. 39 (2005) 1175–1179.
- [21] D.R. Lide, CRC Handbook of Physics and Chemistry, 84th ed., CRC Press, Boca Raton, FL, 2003.
- [22] T. Ang, J. Law, Y.F. Han, Catal. Lett. 139 (2010) 77–84.
- [23] S.Y. Arman, H. Omidvar, S.H. Tabaian, M. Sajjadnejad, S. Fouladvand, S. Afshar, Surf. Coat. Technol. 251 (2014) 162–169.
- [24] G. Mamba, M.A. Mamo, X.Y. Mbianda, A.K. Mishra, Ind. Eng. Chem. Res. 53 (2014) 14329–14338.
- [25] L. Jia, C. Wu, Y. Li, S. Han, Z. Li, B. Chi, J. Pu, L. Jian, Appl. Phys. Lett. 98 (2011) 211903.
- [26] C. Akly, P.A. Chadik, D.W. Mazyck, Appl. Catal. B: Environ. 99 (2010) 329–335.
- [27] C.A. Korologos, C.J. Philippopoulos, S.G. Pouloupoulos, Atmos. Environ. 45 (2011) 7089–7095.
- [28] C.H. Ao, S.C. Lee, J.C. Yu, J. Photochem. Photobiol. A: Chem. 156 (2003) 171–177.
- [29] M. Sleiman, P. Conchon, C. Ferronato, J.M. Chovelon, Appl. Catal. B: Environ. 86 (2009) 159–165.
- [30] R.A.R. Monteiro, F.V.S. Lopes, A.M.T. Silva, J. Ângelo, G.V. Silva, A.M. Mendes, R.A.R. Boaventura, Appl. Catal. B: Environ. 147 (2014) 988–999.
- [31] F. Tang, X. Yang, Build. Environ. 56 (2012) 329–334.
- [32] H.S. Fogler, Elements of Chemical Reaction Engineering, Prentice-Hall, Inc., New Jersey, 2006, pp. 684.
- [33] J. Mo, Y. Zhang, Q. Xu, Appl. Catal. B: Environ. 132 (2013) 212–218.
- [34] T.N. Obee, S.O. Hay, Environ. Sci. Technol. 31 (1997) 2034–2038.
- [35] G.B. Raupp, J.A. Dumesic, J. Phys. Chem. 89 (1985) 5240–5246.
- [36] A. Vittadini, A. Selloni, F. Rotzinger, M. Grätzel, Phys. Rev. Lett. 81 (1998) 2954.
- [37] P.J. Linstrom, W. Mallard, 2001. NIST Chemistry webbook; NIST standard reference database No. 69.
- [38] L. Qiao, J. Chen, X. Yang, J. Environ. Sci. 23 (2011) 51–59.
- [39] N. Watanabe, Astrophys. J. Lett. 571 (2002) L173.

- [40] I. Barnes, K. Becker, N. Mihalopoulos, *J. Atmos. Chem.* 18 (1994) 267–289.
- [41] K. Demeestere, J. Dewulf, B. De Witte, H. Van Langenhove, *Appl. Catal. B: Environ.* 60 (2005) 93–106.
- [42] B.H. Hameed, T.W. Lee, *J. Hazard. Mater.* 164 (2009) 468–472.
- [43] E. Sahle-Demessie, V. G., *Appl. Catal. B: Environ.* 84 (2008) 408–419.
- [44] Z. Wang, J. Liu, Y. Dai, W. Dong, S. Zhang, J. Chen, *Ind. Eng. Chem. Res.* 50 (2011) 7977–7984.
- [45] M. Grandcolas, T. Cottineau, A. Louvet, N. Keller, V. Keller, *Appl. Catal. B: Environ.* 138–139 (2013) 128–140.
- [46] P. Krishnan, M.-H. Zhang, Y. Cheng, D.T. Riag, L.E. Yu, *Constr. Build. Mater.* 43 (2013) 197–202.